In situ synthesis of graphene nitride nanolayers on glycerol-lubricated Si3N4 for superlubricity applications

Y. Long, T. Kuwahara, M.-I. de Barros Bouchet, A. Ristić, N. Dörr, T. Lubrecht, L. Dupuy, G. Moras, J.M. Martin, M. Moseler

ACS APPLIED NANO MATERIALS

www.acsanm.org Article

In Situ Synthesis of Graphene Nitride Nanolayers on Glycerol-Lubricated Si_3N_4 for Superlubricity Applications

Yun Long, Takuya Kuwahara, Maria-Isabel De Barros Bouchet,* Andjelka Ristić, Nicole Dörr, Ton Lubrecht, Laurent Dupuy, Gianpietro Moras, Jean Michel Martin, and Michael Moseler*

Cite This: *ACS Appl. Nano Mater.* 2021, 4, 2721−2732 Read Online

ACCESS | Metrics & More | Article Recommendations | Supporting Information

ABSTRACT: The increasing demand for sustainable tribology has accelerated the development of environmentally friendly lubrication solutions such as water or water-related lubricants. Earlier works have reported on water-lubricated sliding of silicon nitride (Si_3N_4) at high speeds, which can result in a superlow friction ($\mu < 0.01$) owing to the formation of hydrodynamic water films on hydrophilic surface layers. Here, combined boundary-lubrication experiments at low sliding speeds and atomistic simulations reveal an alternative superlubricity mechanism for glycerol-lubricated Si_3N_4. X-ray photoelectron and time-of-flight secondary ion mass spectrometry performed inside and outside the wear track as well as high-resolution mass spectroscopy of the used lubricant strongly suggest that sub-nanometer-thick graphene nitride layers form at the very top of Si_3N_4. In the accompanying atomistic simulations, glycerol molecules undergo tribochemical decomposition and react with surface-bound nitrogen atoms to form carbon nitrides. Further shearing promotes the formation of 2D graphene nitrides that passivate the ceramic surfaces and induce a superlow friction under boundary lubrication. Thus, glycerol-lubricated Si_3N_4 has a high potential for use in green superlubricity enabled by *in situ* synthesis of disordered graphene nitride species.

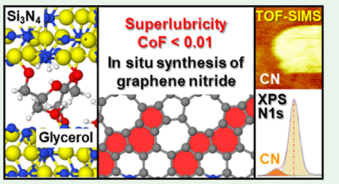

KEYWORDS: *silicon nitride, graphene nitride layers, tribochemistry, boundary lubrication, superlubricity*

INTRODUCTION

Lubrication of ceramic[1] and diamond-like carbon[2] (DLC) coatings with biolubricants represents a sustainable alternative[3] to traditional metallic systems lubricated by non-biodegradable mineral oils combined with toxic traditional additives such as zinc dialkyldithiophosphate. Achieving superlubricity (*i.e.*, coefficient of friction, CoF, $\mu < 0.01$) in such green-lubrication systems is of technological importance for reducing the energy loss and material consumption as well as for minimizing the environmental pollution. Since the pioneering work by Tomizawa and Fischer,[1] friction and wear properties of Si_3N_4 have been extensively examined in water[1,4] and superlubricity was achieved for high-speed water lubrication.[5] The superlow friction was explained by the drastic decrease in the local contact pressure P_N through surface smoothing and the formation of thick hydrodynamic films on hydrophilic silica tribolayers.[6] However, under high normal loads or low speeds (where asperity contacts are dominant), the friction increased significantly due to the breakdown of hydrodynamic lubrication.

While water fails to superlubricate Si_3N_4 under boundary lubrication conditions, nanoparticle-dispersed aqueous solutions[7,8] have shown promising superlubricious potential. Dispersion of nano-additives into water or base oil[9−11] has become a general strategy for the chemical modification of surfaces, for example, silica nano-particles dispersed in water are effective for the formation of a homogeneous silica gel film on the Si_3N_4 surface.[7,8] Another route toward superlubricity of Si_3N_4 employs acidic mixtures of water with glycerol.[6] Luo and co-workers[6] reported boundary superlubricity of Si_3N_4/glass contacts with various acid solutions mixed with glycerol. They explained the superlow friction by a two-step mechanism: acidic solutions with pH < 1.5 can protonate the silica tribolayers, and subsequently, induce the formation of hydrogen-bonded glycerol−water networks on the positively charged silica. Afterward, hydrated water layers form on the glycerol layers. A clear dependence of friction on the pH of acidic solutions[6] led Luo and co-workers[6] to the conclusion that the excellent fluidity of thin hydration layers[12] most likely underlies the observed superlubricity.

Since modern ceramic bearings contain additional steel design elements that are also in contact with the lubricant, tribochemical reactions with acidic lubricants can lead to an early failure of machinery,[13] and therefore, non-acidic water-based lubricant solutions are preferable. An alternative way to achieve superlubricity in boundary lubrication is the *in situ* synthesis of superlubricious carbonaceous tribolayers[14] that would require neither hydrodynamic nor nanoscopic lubricant films between two surfaces in contact. These tribolayers can

Received: December 16, 2020
Accepted: December 31, 2020
Published: February 2, 2021

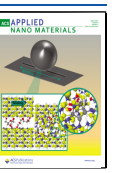

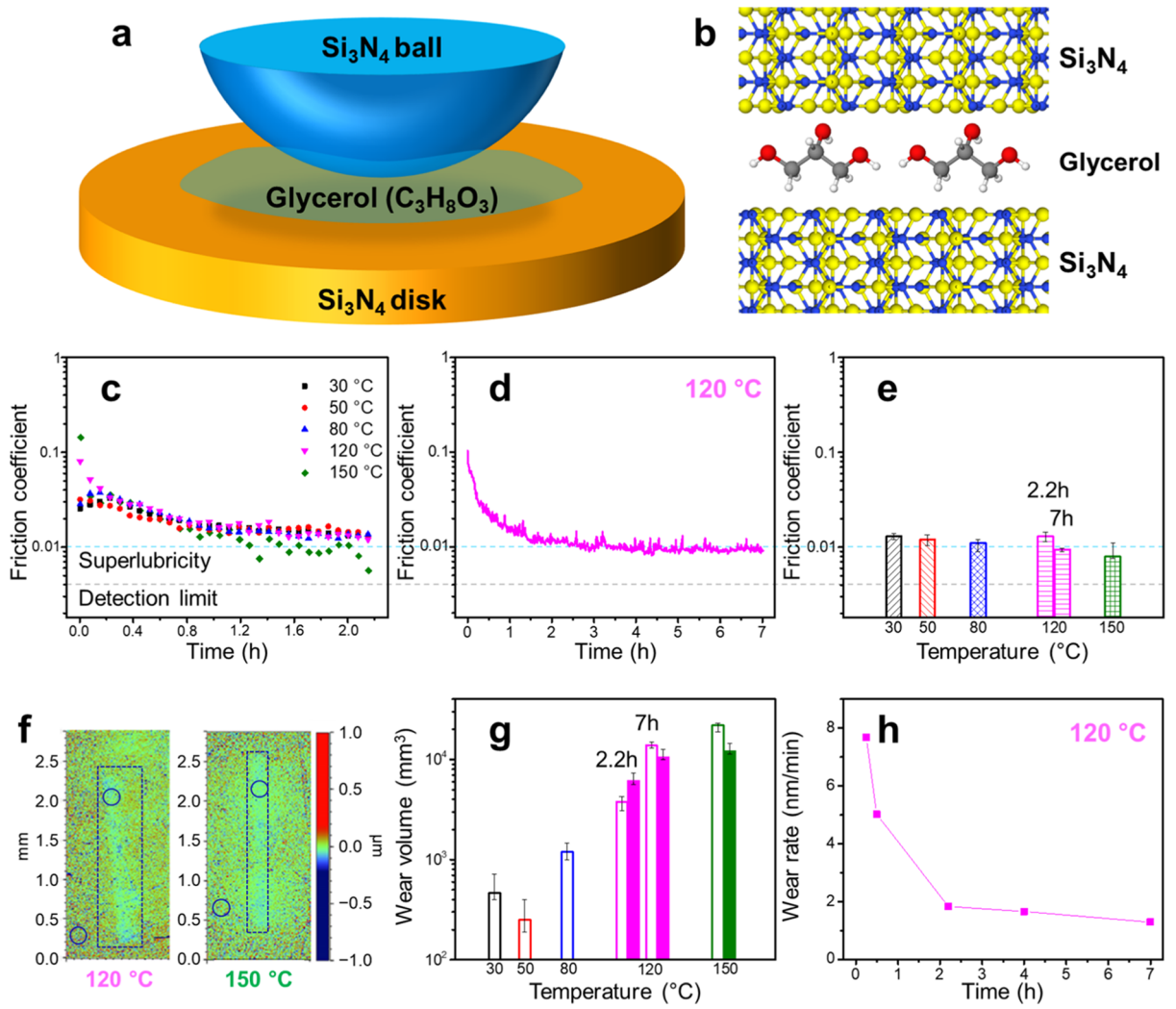

Figure 1. Friction experiments of self-mated Si_3N_4 boundary-lubricated with glycerol. (a) Illustrations of experimental and (b) computational systems studied. (c) Friction curves during 2.2 h sliding for the temperature range T = 30−150 °C. (d) Friction curve during 7 h sliding at T = 120 °C. (e) Final CoFs after 2.2 h sliding for all five temperatures. The final CoF for the 7 h sliding test at T = 120 °C is also plotted in panel (e). (f) Interferometric images of the wear tracks (marked by dashed rectangles) at T = 120 °C (left) and 150 °C (right) showing practically no wear. Ellipses indicate the areas for XPS measurements inside and outside the wear tracks. (g) Final wear volumes after 2.2 h sliding for all five temperatures. The final wear volume for the 7 h sliding at T = 120 °C is also plotted. The wear volumes and CoFs are the medians of three tests for each temperature, and the error bars represent maximum and minimum values. For each test, the final CoF is an average over the last 500 sliding cycles. (h) Evolution of wear (height removal) rate dh/dt (nm/min) in the 7 h sliding test at T = 120 °C in panel (d). The wear rate at time $t = t_i$, $dh/dt|_{t=t_i}$, defined as $2(W_{t_i} - W_{t_{i-1}})/\{(t_i - t_{i-1})\ (A_{t_i} + A_{t_{i-1}})\}$, where $W_{t=t_i}$ and $A_{t=t_i}$ are the wear volume and wear scar area at $t = t_i$, respectively.

form *via* shear-induced structural modifications[15] and reactions of lubricants with solid surfaces.[16] Both processes are observed for boundary-lubricated tetrahedral amorphous carbon (ta-C) and nanocrystalline diamond surfaces. In these materials, ultra-[17,18] and super-low[16,19] friction can be achieved by either a dense surface passivation with hydrogen[20] and hydroxyl functional groups[21] (originating from lubricants) or an aromatic surface passivation due to delocalized π-bonded networks.[2,21,22] The passivation can prevent the formation of chemical bonds across the sliding interface at high contact pressures (GPa), which is a prerequisite for friction reduction. For example, some of the authors utilized tribochemical decomposition of oleic acid to form superlubricious aromatic graphenoid patches on the ta-C surface under boundary[16] and mixed lubrication.[2] Like graphite,[23] aromatic tribolayers are self-lubricating and provide load support at the asperity contact. However, such carbonaceous tribolayers have been exclusively reported in the context of hard carbon coatings, and it is not clear at all if they can form on Si_3N_4 surfaces.

In this article, combined experiments and atomistic simulations demonstrate that the *in situ* formation of sub-nanometer-thick graphene nitrides[24] leads to superlubricity of self-mated Si_3N_4 under boundary lubrication with glycerol over a wide range of temperatures (see illustrations of our experimental and computational systems in Figure 1a,b, respectively). Quantum-mechanical simulations indicate that tribochemical reactions of glycerol with Si_3N_4 preferentially produce two separate phases: amorphous silicon oxide and carbon nitrides. Silicon oxide/hydroxide films are likely to be removed by shear from the direct contact area, whereas carbon nitrides undergo shear-induced phase transitions producing 2D graphene-nitride, adherent tribolayers. Hence, this study proposes a new tribochemical route for achieving green

https://dx.doi.org/10.1021/acsanm.0c03362
ACS Appl. Nano Mater. 2021, 4, 2721−2732

Table 1. Properties of Glycerol and EHL Film Thickness Calculations at Different Temperatures[a]

	temperature T (°C)					
	30	50	80	120	150	120 (7 h)
viscosity (10^{-3} Pa s)	645.8[36]	147.4[36]	31.8[36]	8.3[36]	3.8[36]	8.3[36]
pressure–viscosity coefficient (10^{-9} m^2 N^{-1})	5.9[37]	5.5[37]	5.4[37]	3.6	3.6	3.6
ball wear scar diameter (μm)	101	98	115	148	222	205
average Hertzian contact pressure after sliding (MPa)	387	411	299	180	80	94
ball radius inside the wear scar (μm)	6.9	6.5	10.0	12.3	104	43.5
surface roughness S_a of the ball after sliding (nm)	5.4	5.5	4.8	5.3	3.5	3.1
surface roughness S_a of the disk after sliding (nm)	8.0	8.0	8.0	5.8	5.8	5.5
composite surface roughness after sliding (nm)	9.7	9.7	9.3	7.9	6.8	6.3
EHL film thickness (nm)	12.5	4.3	1.9	0.8	1.8	2.6
lambda ratio before sliding	1.19	0.43	0.15	0.06	0.03	0.06
lambda ratio after sliding	1.28	0.44	0.20	0.10	0.26	0.41

[a]The pressure–viscosity coefficient of glycerol at T = 120 and 150 °C is estimated using that obtained at T = 100 °C.[37]

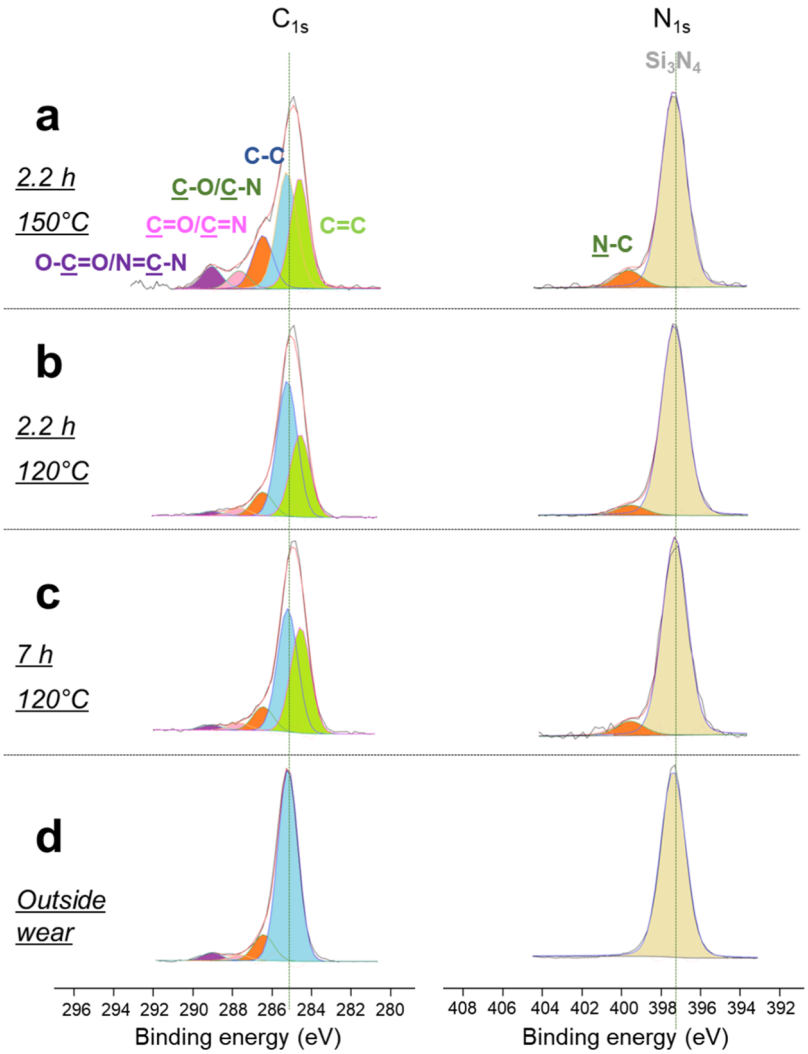

Figure 2. C 1s (left) and N 1s (right) XPS spectra recorded inside the wear tracks on the Si_3N_4 disks (a) at T = 150 °C with the test lasting for 2.2 h, (b) at T = 120 °C with the test lasting for 2.2 h, (c) at T = 120 °C with the test lasting for 7 h, and (d) outside a wear track for comparison.

superlubricity *via* aromatic surface nanolayers on biolubricated Si_3N_4.

RESULTS AND DISCUSSION

Experiments. Friction curves for Si_3N_4 balls sliding against Si_3N_4 disks show similar time evolutions for temperatures ranging from T = 30 to 120 °C (Figure 1c). For all temperatures, the CoF is initially in the range of 0.03–0.08 and converges toward $\mu \approx 0.01$ after 1 h running-in. Most strikingly, when T increases to 150 °C, the CoF decreases more rapidly and ends up at a significantly lower value of μ = 0.008 ± 0.002, which is close to the detection limit of the

https://dx.doi.org/10.1021/acsanm.0c03362
ACS Appl. Nano Mater. 2021, 4, 2721–2732

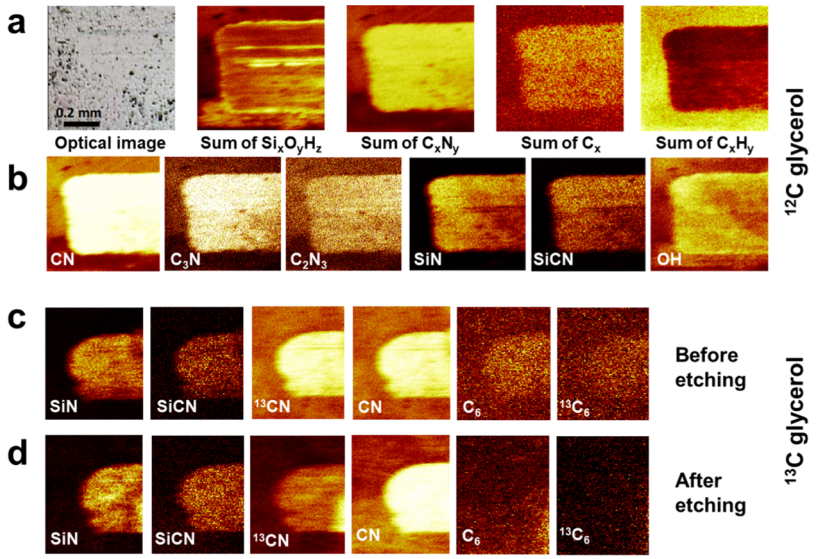

Figure 3. ToF-SIMS chemical maps obtained at the turning point of the Si_3N_4 disk wear track. (a) Selected ToF-SIMS chemical maps for ^{12}C-glycerol lubrication. The corresponding optical image is shown for comparison. (b) ToF-SIMS chemical maps of C_xN_y, Si species, and OH in detail. (c,d) ToF-SIMS chemical maps of the Si_3N_4 disk wear track with ^{13}C-glycerol lubrication (wear track was generated with the same parameters and tribological behavior is consistent with that shown in Figure 1) before (c) and after etching (d).

friction force sensor and characteristic of superlubricious sliding contacts—see, for instance, Figure S1 for the evolution of friction coefficient $\mu(t)$ during the last sliding cycle at 150 °C and compare it with $\mu(t)$ at 120 °C remaining above the superlubricity limit during the whole cycle.

A prolonged 7 h sliding test at T = 120 °C shows that the CoF decreases further and reaches below 0.01 after 3 h of sliding (Figure 1d). This reveals that superlubricity is also achievable (μ = 0.009) at lower temperatures but requires longer running-in periods (which result in a drop of the average Hertzian contact pressure from 180 to 94 MPa, see topographical images on the ball wear scars showing an increase of the wear scar diameter in Figure S2, and an increase in the lambda ratio to 0.4). Final CoFs for 2.2 h sliding at all temperatures are plotted in Figure 1e as well as CoF for 7 h sliding at T = 120 °C. The CoFs are slightly above (all 2.2 h experiments with $T \leq$ 120 °C) or below the superlubricity level (the 2.2 h experiment with T = 150 °C and the 7 h experiment with T = 120 °C).

For all temperatures, wear tracks on Si_3N_4 balls and disks are hardly visible by optical microscopy due to the poor contrast between the inside and outside of the wear track. The wear depth on the Si_3N_4 disk is less than 30 nm for all temperatures (the cases at T = 120 and 150 °C are shown in Figure 1f). This correlates with a wear volume on the order of 10^4 μm^3 (Figure 1g). As for the Si_3N_4 balls, the maximum wear loss detected at T = 150 °C is 2.2×10^4 μm^3. The increase in the wear volumes with temperature follow an Arrhenius behavior (Figure S3), and an estimation of the wear rate dh/dt shows that the wear (even at T = 120 °C) is an atom-by-atom removal process in the superlubricity state (Figure 1h). While dh/dt at T = 120 °C is very high for the first 1 h, it decreases drastically and drops to about 1 nm/min at t = 7 h. Even though worn surfaces are polished after friction, and the ball wear scar diameter has enlarged compared to the initial Hertzian contact diameter, the lambda ratio, that is, the ratio of film thickness[25] to composite surface roughness, stays clearly below unity at T = 150 °C (Table 1). According to general rules in the lubrication regimes, this suggests that the observed superlubricity is not driven by bulk hydrodynamic lubrication or fluid films from elastohydrodynamic lubrication (EHL) and that tribochemical processes triggered by boundary lubrication are crucial (see details in Materials and Methods section).

A series of surface chemical analyses of the worn surfaces shed light on the chemical reactions underlying the observed superlow boundary friction regime. Figure 2 shows spectra obtained by X-ray photoelectron spectroscopy (XPS) carried out inside the wear track on the Si_3N_4 disk for the 2.2 h sliding test at T = 150 °C (Figure 2a) and T = 120 °C (Figure 2b) as well as for the 7 h sliding test at T = 120 °C (Figure 2c). For comparison, XPS spectra outside the wear tracks are shown in Figure 2d. All spectra are calibrated by fixing the Si 2p photopeak of Si_3N_4 at a binding energy (BE) of 101.7 eV.[26] The C 1s XPS spectrum outside the wear track has one major peak at 285.2 eV and a broad shoulder at higher binding energies (Figure 2d). The former is attributed to C−C or C−H bonds (accounting for 88% intensity), while the latter results from C−O, C═O, and O−C═O bonds (small amounts of C−N and C═N bonds are also expected in this energy range). Inside the T = 150 °C wear track, the main peak shifts from 285.2 to 284.8 eV and its width significantly increases (Figure 2a). An additional peak at 284.5 eV BE corresponding to C═C bonds is therefore needed to fit data properly, providing evidence of shear-induced formation of sp^2-hybridized carbon atoms (the carbon sp^2/sp^3 ratio is about 0.82). Intensities of other peaks for C−O/C−N, C═O/C═N, and O−C═O/N−C═N bonds are nearly twice as high as those outside the wear track (see details of the peak fitting in Tables S1 and S2).

A comparison of the N 1s XPS spectra recorded inside (Figure 2a) and outside (Figure 2d) the wear track reveals the tribochemically induced formation of N−C bonds, as evidenced by the peak at 399.6 eV after sliding.[27,28] This peak is 10 times less intense than the Si_3N_4 surface peak (at 397.3 eV), and therefore, the ratio of nitrogen−carbon to nitrogen−silicon bonds is about 0.1. The nitrogen−carbon signal comes either from a carbon nitride surface layer or from

https://dx.doi.org/10.1021/acsanm.0c03362
ACS Appl. Nano Mater. 2021, 4, 2721−2732

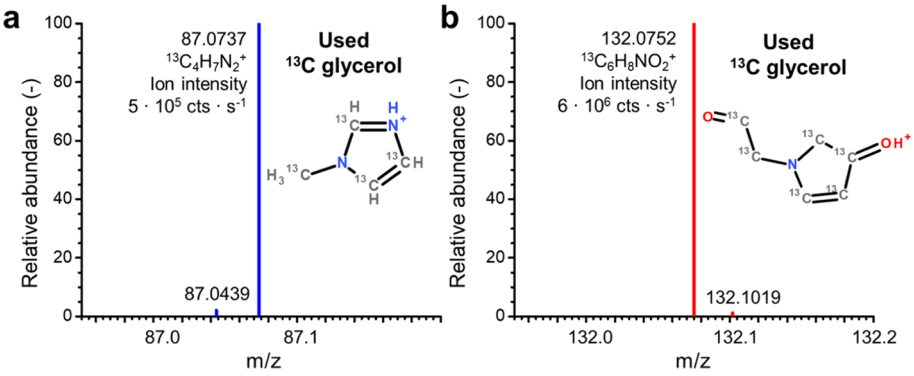

Figure 4. High-resolution mass spectra of used ^{13}C glycerol in positive ion mode obtained by Orbitrap MS. The inset in panel (a,b) displays the ions $^{13}C_4H_7N_2^+$ and $^{13}C_6H_8NO_2^+$ with measured mass/charge (m/z) ratios of m/z 87.0737 and m/z 132.0752, which deviate by 7.4 and 3.3 ppm from calculated m/z 87.0743 and m/z 132.0756, respectively. The intensities 5×10^5 and 6×10^6 (counts s^{-1}) of $^{13}C_4H_7N_2^+$ and $^{13}C_6H_8NO_2^+$, respectively, indicate a high abundance of these ions in the ^{13}C glycerol lubricant after sliding for 2.2 h at T = 150 °C. An additional analysis of ^{13}C glycerol after sliding for 2.2 h at T = 120 °C yields the same species with reduced intensities of 5×10^4 and 1×10^5 (counts s^{-1}) for $^{13}C_4H_7N_2^+$ and $^{13}C_6H_8NO_2^+$, respectively.

some carbon impurities embedded in the Si_3N_4 matrix. However, in the second case, the N−C bonds should be accompanied by the presence of Si−C bonds, which are not detected by XPS analysis. Therefore, most likely, a carbon nitride layer forms at the uppermost surface of the wear scar as a result of the reaction of glycerol with Si_3N_4. As the Si_3N_4 substrate is clearly visible in the XPS spectra, the thickness of the carbon nitride layer should be less than 4.4 nm (see the calculation of the inelastic electron mean free path in the Supporting Information).

Similar C 1s and N 1s XPS spectra are obtained inside the wear track on the Si_3N_4 ball at T = 120 °C after both 2.2 and 7 h sliding (Figure 2b,c, respectively). Interestingly, both C═C and C−N signals are more pronounced after 7 h sliding compared to the 2.2 h test (Figure 2c), indicating a gradual build-up of the carbon nitride layer over many hours.

To better understand the chemical structure of this tribolayer and to quantify its thickness, high-resolution time-of-flight secondary ion mass spectrometry (ToF-SIMS) with a depth resolution of less than 1 nm is performed in exactly the same areas as those of previous XPS analyses of the T = 150 °C wear track. Figure 3a shows an optical image of the track and selected chemical maps generated using emitted ion fragments in the negative mode ($Si_xO_yH_z$, C_xN_y, and C_x). The C_xN_y and C_x ions are more abundant in smoother areas (visible in the upper part of the wear track in the optical image), while the $Si_xO_yH_z$ map is localized in scratches, near the edges, and even outside the track. Figure 3b displays chemical maps of various C_xN_y species present in the spectrum, where the CN, C_3N, and C_2N_3 signals are the most intense. While these C_xN_y fragments are emitted rather evenly from the wear track, SiN, SiCN, and OH are most intense at the turning point of the ball (left part of the wear track in Figure 3b).

The origin of C_xN_y fragments is identified by an additional 2.2 h sliding experiment at T = 150 °C using ^{13}C-labeled glycerol. The experiment with ^{13}C glycerol yields comparable friction behavior and ToF-SIMS intensities as those of ^{12}C glycerol. ToF-SIMS chemical analyses are performed before and after ion-etching of the topmost layer of the worn surface. A comparison of the ToF-SIMS maps before (Figure 3c) and after ion etching (Figure 3d) reveals that the intensities of the CN, SiN, and SiCN maps remain essentially the same, whereas the intensity of the ^{13}CN map significantly decreases after etching. The ^{13}CN, $^{13}C_6$, and C_6 intensities almost vanish after etching. Because the estimated etching depth varies between 0.1 and 1 nm, depending on the material, we suspect that the carbon nitride layers do not have a 3D diamond-like structure but close to a planar 2D structure (possibly disordered).

The nature of chemical bonding of C_xN_y is further elucidated by high-resolution Orbitrap mass spectroscopy (MS) of ^{13}C glycerol collected after sliding. In the used lubricant, the ion $^{13}C_4H_7N_2^+$ (containing an aromatic C_3N_2 ring) at m/z 87.0737 is detected (Figure 4a), while virgin ^{13}C glycerol shows no peak at this m/z. Another peak at m/z 132.0752 indicates the presence of C_4N rings (Figure 4b). As such heterocyclic C_xN_y species were not detected in brass−glycerol−steel sliding contacts,[29] we conclude that tribochemical reactions of glycerol with Si_3N_4 surfaces are likely to produce these cyclic carbon nitrides. In summary, the combination of our XPS, ToF-SIMS, and Orbitrap MS analyses strongly suggests that sub-nanometer-thick carbon nitride layers made of graphenoid structures form at the very top of Si_3N_4 surfaces during sliding under glycerol lubrication.

Simulations. The tribochemical mechanisms underlying the experimentally observed superlubricity of Si_3N_4 and the chemical structure of the carbon nitride tribolayers are explored by density-functional tight-binding[30] (DFTB) molecular dynamics (MD) simulations of glycerol-lubricated β-Si_3N_4. Four glycerol molecules are placed between two β-Si_3N_4 surfaces (initial configuration in Figure 5a, left inset), a normal pressure P_N is applied to the system, followed by sliding MD at constant normal pressure P_N and velocity v. Contact mechanics calculations using experimental white light interferometry topographies reveal maximum local contact pressures of the order of 10 GPa (see the Supporting Information). Therefore, P_N = 10 GPa is used in our simulations. The choice of simulation conditions is further discussed in Materials and Methods.

The simulation shows that the molecules bridge the nanoscopic gap by concurrently chemisorbing on both surfaces (middle inset in Figure 5a) and decompose due to the resulting shear strain. The subsequent cold-welding of the surfaces and mechanical mixing (right inset in Figure 5a) lead to pronounced changes in chemical bonding (see the histogram in Figure 5a). The dissociation of Si−N bonds is the most dominant bond-scission process, producing reactive

https://dx.doi.org/10.1021/acsanm.0c03362
ACS Appl. Nano Mater. 2021, 4, 2721−2732

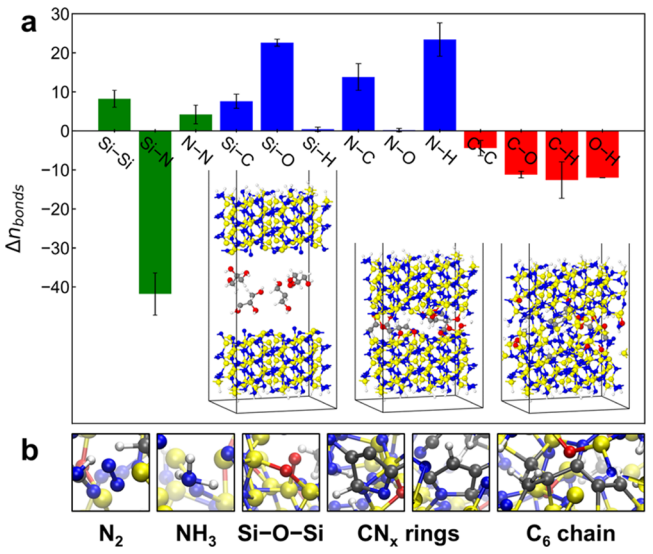

Figure 5. DFTB-MD simulations of β-Si_3N_4 (0001) surfaces in a sliding contact with four glycerol molecules. (a) Changes in the number of chemical bonds in the tribosystems during sliding at T = 300 K. Colors of the bars distinguish the origin of chemical bonds: bonds in Si_3N_4 (green), between Si_3N_4 and glycerol (blue), and in glycerol (red). The numbers are the means over five MD trajectories after 0.2 ns sliding. The error bars represent standard error of the means. The insets show snapshots of a typical MD trajectory at T = 300 K: an initial configuration (left), after pressurization (middle), and after 0.2 ns sliding (right). Yellow, blue, gray, red, and white spheres represent Si, N, C, O, and H atoms, respectively. (b) Zoom-in pictures of representative chemical species and structures observed in the simulations.

Si and N atoms. The following formation of Si−O, N−C, and N−H bonds represent the main bond-formation processes. Almost all glycerol O atoms bind to surface Si atoms, clearly indicating the preferential oxidation of silicon, which is in good agreement with the ToF-SIMS results in Figure 3. Moreover, the number of formed N−C bonds is about two times larger than the number of formed Si−C bonds. This means that carbon binds preferentially to N atoms, in agreement with the experimental evidence for C_xN_y nanolayer formation. Snapshots of representative chemical species (*i.e.*, N_2 and NH_3) and structures (*i.e.*, Si−O−Si bridges, planar CN_x rings, and C_x chains) that form *via* tribochemical reactions are displayed in Figure 5b. The Si−O−Si units and C_xN_y rings are likely precursors of amorphous silica and graphene nitride phases, respectively. For instance, further accumulation and aggregation of dehydrogenated carbon could lead to the formation of large C_xN_y clusters.

Removal of chemical species from the topmost surface layers is crucial for the preferential formation of sub-nanometer-thick C_xN_y tribolayers as accumulated H atoms and silicon oxide would passivate the surfaces and inhibit further chemical reactions of glycerol and N−C bond formation. Our simulations show the generation of small amounts of gaseous species: N_2 molecules are the main chemical products, and NH_3 formation is also observed (Figure 5b). Moreover, ToF-SIMS indicates that silicon oxide/hydroxide layers are transferred from the top of the asperities to neighboring scratches (Figure 3a). As a result, mechanical removal of silicon oxide/hydroxide and detachment of H atoms continuously produce reactive surfaces and promote tribochemical reactions resulting in the formation of sub-nanometer-thick C_xN_y networks.

The experiments and simulations presented so far indicate that the macroscopic frictional behavior is dominated by the shear response of the CN_x phase after its formation. This inspires us to study further structural evolution of this CN_x phase by additional DFTB-MD simulations of bulk N-doped amorphous carbon (a-C:N). Figure 6a−c shows the atomic configurations after 1 ns shearing of a-C:N bulk samples containing different at. % of N. Most strikingly, a-C containing 11 at. % N undergoes a shear-induced phase transition (Figure 6b), also observed for the dry friction of hydrogenated DLC,[15] resulting in a superlow friction regime after running-in (red curve in Figure 6d). Partially nitrogenated, disordered graphene (mainly consisting of five-, six-, and seven-fold rings) forms and covers the entire upper surface (see the top view of Figure 6b). A detailed analysis of the electronic structure of the five-, six-, and seven-fold rings[31] shows that the 2D disordered graphene nitride is highly aromatized (see the top view of Figure 6b, where C atoms belonging to aromatic rings on the lower surface are represented by red spheres).

Nitrogen atoms are incorporated in C_2N and C_3N units similar to those found in ordered graphenoid carbon nitrides (as supported by our ToF-SIMS and Orbitrap MS results). In contrast, shearing pure ta-C does not lead to the formation of graphenoid nanostructures and yields high friction due to cold-welding (Figure 6a,d). Small graphenoid patches are observed in 26 at. % N-doped a-C (Figure 6c), but the surfaces include many non-cyclic defects due to the formation of N_2 molecules and passivating N−C. Apparently, these functional groups inhibit superlow friction (blue curve in Figure 6d) as the excess nitrogen disturbs shear-induced aromatization of a-C:N layers. Indeed, the chemical composition and structure of the graphenoid layer are far from those of graphene nitride (g-C_3N_4).[32] The results indicate the existence of a window of N content that enables shear-induced aromatization of a-C:N layers.

Shear induces sp^3-to-sp^2 rehybridization of carbon atoms near the sliding interface. However, as shown in the result of pure a-C (Figure 6a), the shear-induced sp^3-to-sp^2 rehybridization alone cannot produce a lubricious graphene compound. Carbon atoms undergo rehybridization between sp^2 and sp^3 continuously under shear. In contrast, a small amount of nitrogen atoms incorporated into a-C matrices plays a crucial role in the phase transition from a 3D diamond-like to 2D aromatic planar structure. Due to its lower valency, nitrogen can open the local structure resulting in the formation of isolated planar rings and also passivate dangling bonds of nearest-neighbor carbon atoms. When nitrogen is localized in a narrow zone under mechanical mixing, a larger aromatic graphene plane can be generated (Figure 6b). Interestingly, this doping effect is not limited to nitrogen, as also oxygen-doped ta-C transforms into disordered graphene oxide under shear.[16]

Both graphene nitrides and graphene oxides[16] observed in our atomistic tribosimulations are anchored by a few out-of-plane C−C bonds to the underlying substrate, resulting in a slight out-of-plane corrugation of the 2D graphenoid arches between the anchoring points (Figure 6). While the small corrugation and the disordered structure of the graphenoid layer observed for 11 at.% N-doping (Figure 6b) do not hinder superlubricity (see the red curve in Figure 6d), the higher structural corrugation at 26 at. % N-doping in combination

https://dx.doi.org/10.1021/acsanm.0c03362
ACS Appl. Nano Mater. 2021, 4, 2721−2732

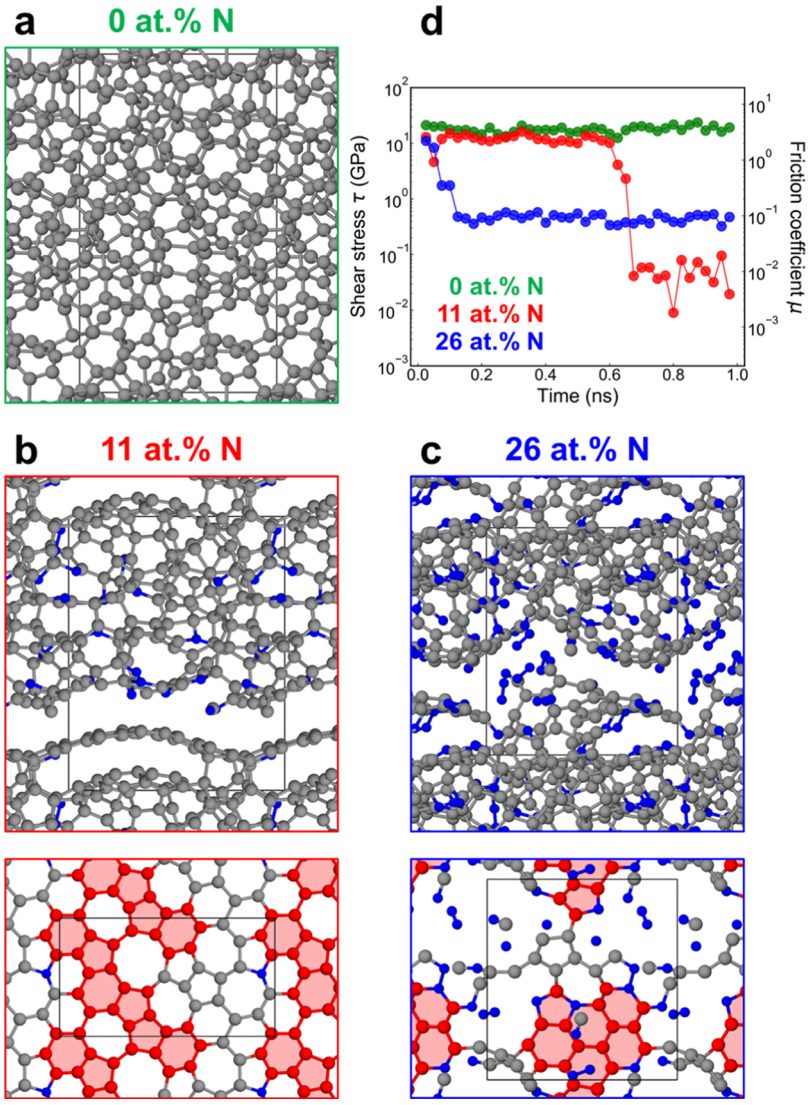

Figure 6. DFTB-MD shearing simulations of pure and N-doped bulk ta-C using Lees–Edwards boundary conditions and v = 100 m s^{-1}. (a) Side view of the atomic configuration at t = 1 ns for pure ta-C. (b,c) Side and top views of the atomic configurations at t = 1 ns for N-doped ta-C with 11 and 26 at. % N, respectively. For the top views, the lower surfaces at the sliding interfaces are displayed. The C atoms belonging to aromatic rings are represented by red spheres. Aromaticity indices I_a of five-, six-, and seven-fold rings are evaluated based on a multicenter bond order analysis.[31] For $I_a > 10^{-2}$, we consider a ring aromatic. (d) Time evolution of the shear stress τ_{zx} and CoF $\mu = \tau_{zx}/P_{ext}$.

with additional functional nitrogen groups (Figure 6c) leads to increased friction (blue curve in Figure 6d), most likely due to a rougher potential energy landscape.[20]

So far, superlubricity of Si_3N_4 has been explained by the easy shearing of bulk hydrodynamic or nanoscopic water layers between hydrophilic colloidal silica or silica gel tribofilms that form during tribochemical reactions of water with Si_3N_4. In our case, ToF-SIMS results show that silicon hydroxide is also formed but does not concentrate directly on the contact area but in scratches and the contact edge. Therefore, the superlubricity phenomenon presented here is not thought to rely on silica formation and water film lubrication, but instead is achieved through the *in situ* synthesis of self-lubricating 2D graphene nitrides.

The actual superlubricity mechanism can be selected through a suitable choice of lubricant and loading conditions. For instance, using water solutions with low pH mixed with glycerol results in superlubricity by silica–water layers, while the use of pure glycerol reduces the formation of surface silicon oxide and has the potential to trigger superlubricity by graphene nitrides as in our case. The results of DFTB-MD simulations indicate that significant proportions of tribochemical reaction products form graphene-type structures. Interestingly, the graphene nitride/graphene superlubricity reported in this work has been achieved under much more severe boundary lubrication conditions (*i.e.*, at v_{max} = 3 mm s^{-1} and even lower speeds, as shown in Figure S4a, and $\lambda \ll 1$, see Table 1) than in previous studies[5,6] on silica–water-layer superlubricity. For example, at T = 150 °C, the viscosity of glycerol is close to that of water, and the initial lambda λ of 0.03 means that most asperities are in contact and experience high contact pressures (Figure S5). Under such severe conditions, bulk hydrodynamic lubrication and EHL by glycerol are excluded and the tribochemical synthesis of graphene nitrides is promoted by large contact pressure and shear stress at the asperity contacts. Under much more moderate lubrication conditions, glycerol can form a hydrodynamic film between two sliding surfaces.[6] Given the absence

https://dx.doi.org/10.1021/acsanm.0c03362
ACS Appl. Nano Mater. 2021, 4, 2721–2732

of asperities (atomically flat surfaces) while keeping the other conditions of our contact unaltered, the glycerol nano-film in the contact would be almost isoviscous because of the increase of the contact radius inside the wear scar (corresponding to significant decrease in the contact pressure) and the low viscosity−pressure coefficient of glycerol. For these unrealistic conditions, the CoF is calculated well below 10^{-4} (see Figure S4b). This clearly demonstrates that contacts between asperities are mainly responsible for the experimental CoF value of 0.006. Therefore, the graphene nitride/graphene superlubricity reported in this article is certainly beneficial for engineering applications that operate under extreme lubrication conditions including mechanical seals, roller bearings, and piston rings.

CONCLUSIONS

This study unveils that the *in situ* tribosynthesis of sub-nanometer-thick graphene nitride layers establishes a superlubricity regime for Si_3N_4 under boundary lubrication with glycerol—see the schematic diagrams showing the running-in processes that are necessary for achieving superlubricity in Figure 7. Initial severe contacts of rough Si_3N_4 surfaces cause

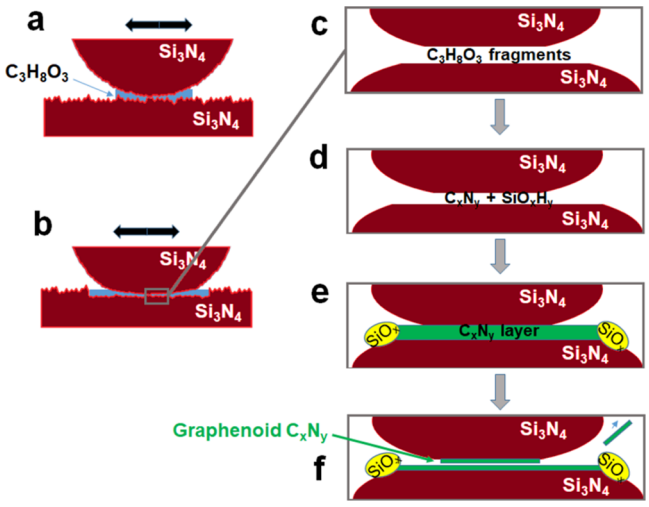

Figure 7. Schematic diagrams for achieving superlubricity of Si_3N_4 boundary lubricated with glycerol by *in situ* synthesis of graphene nitride nanolayers. (a) Initial sliding contact of a Si_3N_4 ball and disk. (b) Plastic deformation of the ball and the resulting increase in the Hertzian contact area. (c−f) Asperity-scale illustration of tribochemical processes occurring at the sliding interface of Si_3N_4/glycerol/Si_3N_4. (c) Decomposition of glycerol, (d) formation of C_xN_y and silicon oxide/hydroxide (SiO_xH_y) phases. (e) Mechanical removal of the SiO_xH_y layer and formation of a nm-thick C_xN_y layer. (f) Shear-induced formation of a 2D aromatic graphene nitride nanolayer.

plastic deformation of surface asperities (Figure 7a→b), resulting in an increase of the apparent contact area (wear scar) and a decrease in the surface roughness. Both are crucial to ease the severe lubrication condition by decreasing the macroscopic Hertzian pressure and nanoscopic local contact pressures in asperity contact spots. Meanwhile, high local contact pressures (>10 GPa) accelerate the decomposition of glycerol at the sliding interface (Figure 7c). The tribochemical reactions of glycerol with Si_3N_4 produce two chemical phases of CN_x and SiO_xH_y (Figure 7d). A nanometer-thick CN_x layer forms homogeneously on the surface, whereas SiO_xH_y species are transported to edges and outside the wear track under shear owing to their poor mechanical properties (Figure 7e). Moreover, shear induces a phase transition of the CN_x layer to 2D aromatic graphene nitride (Figure 7f). A resulting drastic decrease in the shear stress by 2−3 orders of magnitude leads to superlubricity (despite the increase in the contact area). After reaching the superlubricity state, the system is in dynamic equilibrium between detachment of graphene nitride nanolayers (accompanied by atom-by-atom wear) and formation of a new graphenoid layer.

The continuous involvement of surface-bound N atoms is essential for promoting aromatization, and thus passivation, of the topmost atomic surface layer. The graphene nitride/graphene compounds are able to support high contact pressures and help to form a superlubricious interface under severe boundary lubrication conditions. These findings pave the way for the utilization of *in situ* tribochemical synthesis of graphenoid compounds on silicon-based ceramics to achieve green superlubricity. Moreover, it stimulates further research that considers the use of other biolubricants and investigates the lubrication conditions that make the structure of aromatic tribolayers controllable and their formation on other ceramic interfaces (*e.g.*, dry Si_3N_4/a-CN_x) possible.

MATERIALS AND METHODS

Materials. Glycerol $^{12}C_3H_8O_3$ (≥99.5%) and isotopically labeled glycerol $^{13}C_3H_8O_3$ (99%) were purchased from Sigma-Aldrich (St. Louis, USA) and Cambridge Isotope Laboratories (Tewksbury, USA), respectively. Si_3N_4 balls with a diameter of 12.7 mm were provided by CIMAP (Paris, France). Si_3N_4 disks were produced by LianYunGang HighBorn Technology Co. (Lianyungang, China). All ceramic materials were produced by hot pressure sintering and their properties are listed in Table S3. As detected by energy-dispersive X-ray spectroscopy (EDS), impurities based on C, Al, O, and Y originate from the presence of alumina, silica, and yttria in the binder of Si_3N_4. D and G peaks of carbon are not observed by Raman spectroscopy (Figure S6), indicating the absence of graphitic carbon.[33]

Friction and Wear Experiments. Sliding experiments were conducted on a homemade linear reciprocating tribometer with a ball-on-disk configuration (Figure S7). All virgin specimens were thoroughly cleaned by ultrasonication in *n*-heptane for 30 min, followed by acetone for 5 min. Before pairing the ball and disk, a sufficient amount (50 μL) of glycerol was placed with a syringe on the disk. The loss by reactions with Si_3N_4 surfaces is negligible. Experiments were performed in a wide temperature range T = 30−150 °C for a duration of 2.2 h. The sliding test at T = 120 °C was prolonged to 7 h to investigate if the same superlubricity as that at T = 150 °C is achievable at a lower temperature. The flash temperature rise at all temperatures is less than 0.1 °C (see the Supporting Information).

The relative humidity for all experiments is around 25%, which indicates that glycerol absorbs water from air (about 5 wt % at 30 to 100 °C and less for 150 °C due to water evaporation[34]). This could result in a contribution of the water-nanolayer mechanism to our observed superlubricity. However, Chen *et al.*[35] observed water-nanolayer-induced superlubricity in glycerol-lubricated steel contacts only for relative humidity between 40 and 50%, well above the level of humidity in our experiments.

To ensure that the contact surfaces are not fully separated by liquid films at all temperatures, that is, to establish the boundary lubrication, the following tribological conditions were chosen: a maximum sliding speed of 3 mm s^{-1} and a normal load of 3.1 N, corresponding to an initial maximum Hertzian contact pressure P_{max} = 0.75 GPa and an initial Hertzian contact diameter of about 90 μm. The stroke length was fixed at 2 mm to guarantee a long kinematic length. Elasto-hydrodynamic central lubrication film thicknesses calculated by the Nijenbanning−Venner−Moes equation[25] (see the following section) and lambda ratios are listed in Table 1. The viscosity and pressure−

https://dx.doi.org/10.1021/acsanm.0c03362
ACS Appl. Nano Mater. 2021, 4, 2721−2732

viscosity coefficient of glycerol are taken from the literature.[36,37] The accuracy of the measured CoF was ±0.002. Each friction experiment was repeated three times and showed good repeatability (see Figure S8).

Central Film Thickness Calculations. The lubricant film thickness is calculated using the Nijenbanning–Venner–Moes[25] equation for EHL of a ball-on-flat contact. The central film thickness h_{center} is estimated by

$$h_{centre} = r_x(2U)^{0.5} ((H_{RI}{}^{3/2} + (H_{EI}{}^{-4} + H_{00}{}^{-4})^{-3/8})^{2s/3} + (H_{RP}{}^{-8} + H_{EP}{}^{-8})^{-s/8})^{1/s} \quad (1)$$

with $s = 1.5(1 + e^{-1.2/H_{EI}/H_{RI}})$. Here, r_x is the radius of curvature parallel to the sliding direction and the other numbers U, H_{00}, H_{RI}, H_{EI}, H_{RP}, and H_{EP} are given in Table 2. The actual lubrication regimes

Table 2. Dimensionless Numbers Entering the Nijenbanning–Venner–Moes[25] Formula[a]

$H_{00} = 1.8D^{-1}$	$L = G(2U)^{0.25}$
$H_{RI} = 145(1 + 0.796D^{14/15})^{-15/7}D^{-1}M^{-2}$	$M = W/(2U)^{0.75}$,
$H_{EI} = 3.18(1 + 0.006 \ln D + 0.63D^{4/7})^{-14/15}D^{-1/15}M^{-2/15}$	$G = \alpha E'$
$H_{RP} = 1.29(1 + 0.691D)^{-2/3}L^{2/3}$	$U = \eta_0 u/E' r_x$
$H_{EP} = 1.48(1 + 0.006 \ln D + 0.63D^{4/7})^{-7/20}D^{-1/24}M^{-1/12}L^{3/4}$	$W = w/(E' r_x^2)$,

[a]Here, α, η_0, u, and w are the pressure–viscosity coefficient, lubricant dynamic viscosity, sliding speed, and applied normal load, respectively. The reduced Young's modulus E' and the reduced radius of curvature D are calculated from $1/E' = 2((1 - \upsilon_A^2)/E_A + (1 - \upsilon_B^2)/E_B)$ and $D = r_x/r_y$, respectively. E and ν are the elastic modulus and Poisson's ratio, respectively. r_y is the radius of curvature perpendicular to the sliding direction.

are determined by evaluating the dimensionless lambda parameter, which is defined as the ratio between the central film thickness and the combined roughness of the two surfaces

$$\lambda = h_{centre}/\sqrt{R_{RMS,pin}{}^2 + R_{RMS,disk}{}^2} \quad (2)$$

When $\lambda < 1$, the system is in boundary lubrication and its tribological behavior is dominated by physical/chemical interactions between two contacting asperities. The viscosity of the lubricant does not affect the friction coefficient. As λ increases, the friction regime changes to mixed ($1 < \lambda < 3$) and hydrodynamic ($\lambda > 3$) lubrication regimes, where the lubricant viscosity significantly influences the CoF. The calculated lambda values (Table 1) at T = 120 and 150 °C are well below unity, which confirms that the observed superlubricity is attributed to the formation of graphene nitride nanolayers, not to hydrodynamic films.

Surface Chemical Analyses. Specimens were carefully cleaned with water and dried in a stove at T = 80 °C to eliminate residual glycerol at the end of the experiments. In this study, we did not employ ultrasonic cleaning since it could have changed the chemical structures of the rubbed surfaces. Digital microscopy (VHX-1000, Keyence, Osaka, Japan) was used to image wear tracks. Interferometry (ContourGT-X, Bruker, Billerica, USA) was employed to obtain the topography of wear tracks. Considering that the production process leaves a large number of pores in the ceramic specimens, the root-mean-square surface roughness S_a was calculated by ignoring all negative heights. A scanning electron microscope equipped with an EDS system (MIRA3, TESCAN, Fuveau, France) was operated under an acceleration voltage V = 5 keV and a dead time of 30% to determine the chemical compositions of the virgin specimens. Raman spectroscopy (LabRam 800, Horiba Scientific, Jobin Yvon, France) was specially used to detect carbon impurities and their structures in the virgin specimens. Therefore, Raman spectra were recorded using a 633 nm laser beam.

An XPS spectrometer (ULVAC-PHI Versa Probe II spectrometer) with an Al K_α X-ray source was used to observe the chemical changes on the top surfaces. The take-off angle was set to 45°. In order to make sure that the analysis area was well located inside wear tracks, the analysis area was fixed at 50 × 50 μm^2. The information depth of XPS analyses is elucidated in the Supporting Information.

ToF-SIMS (ToF-SIMS 5, IONTOF, Münster, Germany) with a Bi ionization source and an excitation voltage of 25 kV was applied to probe the topmost molecular layer of about 1 nm of the disk specimens. A high mass resolution (around 10,000 at m/z 28) mode was chosen to distinguish molecular ions with very close masses. The area for spectroscopic analysis was 100 × 100 μm^2, while the area for chemical mapping was extended to 500 × 500 μm^2.

Lubricant Analyses. Linear trap quadrupole Orbitrap XL hybrid tandem mass spectrometer (Orbitrap MS, ThermoFisher Scientific, Bremen, Germany) provided an insight into the chemical reaction products formed in the sliding contact and released into glycerol during the friction and wear experiments at T = 120 and 150 °C. Structural identification was based on the collection of glycerol from disks after the experiments and dissolution in methanol (≥99.9%, Chromasolv grade), followed by direct infusion without prior chromatographic separation, modified from a method for zinc dialkyl dithiophosphate.[38,39] Orbitrap MS analyses were carried out in the positive ion mode using electrospray ionization. In the linear ion trap analyzer, low-energy collision-induced dissociation was performed for the structural identification by tandem MS. Full scan mass spectra in the m/z range 50–1000 and tandem mass spectra were acquired with an Orbitrap analyzer with high resolution of typically R = 60,000 at full width at half maximum at m/z 400. All measurements were acquired with a mass accuracy of 15 ppm or better, based on an external calibration method. Data processing and interpretation were performed using software tools Xcalibur version 2.0.7 and Mass Frontier version 6.0 (ThermoFisher Scientific, Bremen, Germany).

Quantum-Mechanical MD Simulations. Tribochemical reactions occurring at self-mated Si_3N_4 sliding surfaces with glycerol were studied by self-consistent-charge density-functional tight-binding molecular dynamics (SCC-DFTB MD) simulations,[30] as implemented in the Atomistica package. The Slater–Koster parameters were well tested, especially for Si_3N_4 surfaces,[40] silica/diamond tribosystems,[41] and amorphous carbon/glycerol tribosystems.[16] The system consists of two β-Si_3N_4 (0001) slabs in a unit cell with 15.62 × 13.52 × 50.00 Å^3 with four free glycerol molecules between the slabs. The dangling bonds of atoms in the outermost layers were terminated with hydrogen atoms, while those at the interface were not terminated. The two outermost layers and terminating hydrogen atoms were kept rigid. The temperature T in the entire system was kept constant at 300 and 423 K using a Langevin thermostat[42] except for the rigid atoms. The equations of motion were integrated with Δt = 0.5 fs using the velocity Verlet algorithm.[42] A normal pressure P_N of 10 GPa was applied to the topmost rigid layers. After reaching an equilibrium state under the external pressure, a constant sliding velocity v of 100 m s^{-1} was added along the x direction while keeping the normal pressure using the Pastewka–Moser–Moseler pressure-coupling barostat.[43] Five independent MD trajectories were generated for each temperature to ensure the repeatability of our results. Moreover, shearing simulations of amorphous carbon nitride bulks at a sliding speed v_x = 100 m s^{-1} were carried out for 1 ns using Lees–Edwards boundary conditions,[44] which are widely employed in non-equilibrium MD simulations to impose a shear flow in a representative volume element of a bulk condensed matter system. The system temperature was kept constant at T = 300 K using the Peters thermostat,[45] and the Berendsen barostat[46] with P_{ext} = 5 GPa was applied in all three directions. Amorphous carbon nitride samples were generated by rapidly quenching carbon nitride melts from 5000 to 0 K. The short-time averaged shear stress was calculated from the τ_{zx} component of the stress tensor. Visualization was carried out with the open-source softwares VMD[47] and OVITO.[48]

The applied normal pressure P_N of 10 GPa in the sliding MD simulations is higher than the macroscopic Hertzian contact pressures after sliding (*e.g.*, 80 MPa for T = 150 °C, see Table 1). This choice

https://dx.doi.org/10.1021/acsanm.0c03362
ACS Appl. Nano Mater. 2021, 4, 2721–2732

was made because major asperities experience contact pressures that are much larger than the Hertzian pressure upon asperity collisions under severe boundary lubrication conditions. Especially, for hard Si_3N_4, a local contact pressure is likely to reach values on the order of 10 GPa. For instance, in contact mechanics calculations using the Hertzian contact pressures (Table 1) as well as the ball and disk topographies after running-in at T = 150 °C, approximately 9.6% of the real contact area experience a local normal pressure of 10 GPa and more (see Figure S5).

As in most MD studies, the limitation in computational resources and the relatively high computational cost of DFTB-MD simulations make simulations at our experimental sliding speeds practically impossible. In this study, a sliding speed v = 100 m s^{-1} (several orders of magnitude higher than the experimental one) was used in order to simulate a long sliding distance and to sufficiently sample phase space within the simulation time ($t_{max} \leq$ 1 ns). For a physically sound modeling of tribological interfaces, the sliding speed must be much lower than the speed of sound in materials. This ensures that the heat generated in contact during sliding is rapidly dissipated from the sliding interface to the surrounding material, which was modeled by coupling all atoms with a heat bath in our simulations. The speed of sound in Si_3N_4 ($\sim 7 \times 10^3$ m s^{-1})[49] is much higher than the sliding speed in our simulations.

Although the rate of chemical reactions in our simulations is higher than in the experiment, we confirmed that the reaction products are independent of the sliding speed. Previous quasi-static sliding simulations (in the limit of $v \rightarrow 0$ m s^{-1}) and MD (at v = 100 m s^{-1}) confirm that the reaction pathways in strongly bonded covalent materials hardly depend on the sliding speed[16] and suggest that our simulation results are transferable to low-speed experiments. Especially at low temperatures ($kT \ll 1$ eV), reactions are hardly affected by thermal vibrations of chemical bonds and are predominantly activated by mechanical work. The reaction products are fully determined by the competition between the mechanical strength and stiffness for different types of chemical bonds. This argument is corroborated by the excellent agreement in chemical bond analyses between our experiments (Figures 2 and 3) and simulations (Figure 5).

■ ASSOCIATED CONTENT

Supporting Information

The Supporting Information is available free of charge at https://pubs.acs.org/doi/10.1021/acsanm.0c03362.

Last friction cycle after 2.2 h testing at T = 120 and 150 °C; topographical images of Si_3N_4 ball wear scars after 2.2 and 7 h sliding; wear volumes as a function of $1/k_BT$; fitting details for C 1s XPS spectra; fitting details for N 1s XPS spectra; information depth calculation of N_{1s} peak; friction curve of self-mated Si_3N_4 in glycerol at T = 150 °C; theoretical CoF originating from shearing glycerol at T = 150 °C as a function of speed; contact mechanics calculations; contact mechanics calculations of Si_3N_4 topographies by interferometry inside a wear track after sliding at T = 150 °C; Raman spectrum of a Si_3N_4 virgin disk; mechanical properties and chemical compositions of virgin Si_3N_4 materials; picture of a homemade reciprocating tribometer; flash temperature calculations; flash temperature rise of tests at each temperature; and friction curves of all reciprocating sliding tests at T = 30−150 °C (PDF)

■ AUTHOR INFORMATION

Corresponding Authors

Maria-Isabel De Barros Bouchet − *Laboratory of Tribology and System Dynamics, University of Lyon, Ecole Centrale de Lyon, CNRS UMR 5513, Ecully 69134, France*; Email: maria-isabel.de-barros@ec-lyon.fr

Michael Moseler − *Fraunhofer Institute for Mechanics of Materials IWM, MicroTribology Center μTC, Freiburg 79108, Germany; Institute of Physics, Freiburg Materials Research Center, and Cluster of Excellence livMatS, Freiburg Center for Interactive Materials and Bioinspired Technologies, University of Freiburg, Freiburg 79104, Germany*; Email: michael.moseler@iwm.fraunhofer.de

Authors

Yun Long − *Laboratory of Tribology and System Dynamics, University of Lyon, Ecole Centrale de Lyon, CNRS UMR 5513, Ecully 69134, France*

Takuya Kuwahara − *Fraunhofer Institute for Mechanics of Materials IWM, MicroTribology Center μTC, Freiburg 79108, Germany*; orcid.org/0000-0002-4859-6654

Andjelka Ristić − *AC2T research GmbH, Wiener Neustadt 2700, Austria*

Nicole Dörr − *AC2T research GmbH, Wiener Neustadt 2700, Austria*

Ton Lubrecht − *LaMCoS, Université de Lyon, INSA de Lyon, CNRS 5259, Villeurbanne F69621, France*

Laurent Dupuy − *Science Et Surface, Ecully F69134, France*

Gianpietro Moras − *Fraunhofer Institute for Mechanics of Materials IWM, MicroTribology Center μTC, Freiburg 79108, Germany*; orcid.org/0000-0002-4623-2881

Jean Michel Martin − *Laboratory of Tribology and System Dynamics, University of Lyon, Ecole Centrale de Lyon, CNRS UMR 5513, Ecully 69134, France*

Complete contact information is available at: https://pubs.acs.org/10.1021/acsanm.0c03362

Author Contributions

Y.L. and T.K. contributed equally to this work. M.-I.D.B.B., J.M.M., and M.M conceived and supervised the research. Y.L. designed and performed the friction experiments and conducted the XPS analyses. L.D. performed the ToF-SIMS analyses. A.R. and N.D. performed the Orbitrap MS analyses. T.L. performed the surface roughness measurements. T.K., G.M., and M.M. designed the simulations. T.K. performed the simulations. Y.L., T.K., M.-I.D.B.B, N.D., G.M., J.M.M., and M.M. interpreted the findings and wrote the manuscript. All authors discussed the results and approved the final version of the manuscript.

Funding

M.-I.D.B.B. and J.M.M. wish to express their acknowledgement to the Agence Nationale de la Recherche (ANR) for partial funding of the ULVAC-PHI Versa Probe II XPS spectrometer. The experimental research part of work was also supported by TOTAL, Solaize Researcher Center. T.K., G.M., and M.M. gratefully acknowledge funding from the BMWi (Bundesministerium für Wirtschaft und Energie) within the project Poseidon II. Orbitrap MS analyses were supported by the Austrian COMET-Program (K2 project InTribology, no. 872176) and carried out at the "Excellence Centre of Tribology" (AC2T research GmbH).

Notes

The authors declare no competing financial interest.

https://dx.doi.org/10.1021/acsanm.0c03362
ACS Appl. Nano Mater. 2021, 4, 2721−2732

■ ACKNOWLEDGMENTS

Computing time was granted by the John von Neumann Institute for Computing (NIC) and provided on the supercomputer JUWELS[50] at Jülich Supercomputing Centre (JSC) within the project HFR09. Further computing time was provided by the State of Baden-Württemberg through bwHPC and the DFG (grant no. INST 39/963-1 FUGG, bwForCluster NEMO). We thank Melissa Stoll for conducting the contact mechanics calculations.

■ REFERENCES

(1) Tomizawa, H.; Fischer, T. E. Friction and Wear of Silicon Nitride and Silicon Carbide in Water: Hydrodynamic Lubrication at Low Sliding Speed Obtained by Tribochemical Wear. *ASLE Trans.* **1987**, *30*, 41−46.

(2) De Barros Bouchet, M. I.; Martin, J. M.; Avila, J.; Kano, M.; Yoshida, K.; Tsuruda, T.; Bai, S.; Higuchi, Y.; Ozawa, N.; Kubo, M.; Asensio, M. C. Diamond-like Carbon Coating under Oleic Acid Lubrication: Evidence for Graphene Oxide Formation in Superlow Friction. *Sci. Rep.* **2017**, *7*, 46394.

(3) Zhang, S.-w. Green Tribology: Fundamentals and Future Development. *Friction* **2013**, *1*, 186−194.

(4) Chen, M.; Kato, K.; Adachi, K. Friction and Wear of Self-Mated SiC and Si_3N_4 Sliding in Water. *Wear* **2001**, *250*, 246−255.

(5) Chen, M.; Kato, K.; Adachi, K. The Comparisons of Sliding Speed and Normal Load Effect on Friction Coefficients of Self-Mated Si_3N_4 and SiC under Water Lubrication. *Tribol. Int.* **2002**, *35*, 129−135.

(6) Li, J.; Zhang, C.; Ma, L.; Liu, Y.; Luo, J. Superlubricity Achieved with Mixtures of Acids and Glycerol. *Langmuir* **2013**, *29*, 271−275.

(7) Lin, B.; Ding, M.; Sui, T.; Cui, Y.; Yan, S.; Liu, X. Excellent Water Lubrication Additives for Silicon Nitride to Achieve Superlubricity under Extreme Conditions. *Langmuir* **2019**, *35*, 14861−14869.

(8) Cui, Y.; Ding, M.; Sui, T.; Zheng, W.; Qiao, G.; Yan, S.; Liu, X. Role of Nanoparticle Materials as Water-Based Lubricant Additives for Ceramics. *Tribol. Int.* **2020**, *142*, 105978.

(9) Zeng, Q.; Yu, F.; Dong, G. Superlubricity Behaviors of Si3N4/DLC Films under PAO Oil with Nano Boron Nitride Additive Lubrication. *Surf. Interface Anal.* **2013**, *45*, 1283−1290.

(10) Joly-Pottuz, L.; Dassenoy, F.; Belin, M.; Vacher, B.; Martin, J. M.; Fleischer, N. Ultralow-Friction and Wear Properties of IF-WS2 under Boundary Lubrication. *Tribol. Lett.* **2005**, *18*, 477−485.

(11) Wang, W.; Xie, G.; Luo, J. Black Phosphorus as a New Lubricant. *Friction* **2018**, *6*, 116−142.

(12) Raviv, U.; Klein, J. Fluidity of Bound Hydration Layers. *Science* **2002**, *297*, 1540−1543.

(13) Kaczorowski, D.; Combrade, P.; Vernot, J. P.; Beaudouin, A.; Crenn, C. Water Chemistry Effect on the Wear of Stainless Steel in Nuclear Power Plant. *Tribol. Int.* **2006**, *39*, 1503−1508.

(14) Erdemir, A.; Ramirez, G.; Eryilmaz, O. L.; Narayanan, B.; Liao, Y.; Kamath, G.; Sankaranarayanan, S. K. R. S. Carbon-Based Tribofilms from Lubricating Oils. *Nature* **2016**, *536*, 67−71.

(15) Chen, X.; Zhang, C.; Kato, T.; Yang, X.-a.; Wu, S.; Wang, R.; Nosaka, M.; Luo, J. Evolution of Tribo-Induced Interfacial Nanostructures Governing Superlubricity in a-C:H and a-C:H:Si Films. *Nat. Commun.* **2017**, *8*, 1675.

(16) Kuwahara, T.; Romero, P. A.; Makowski, S.; Weihnacht, V.; Moras, G.; Moseler, M. Mechano-Chemical Decomposition of Organic Friction Modifiers with Multiple Reactive Centres Induces Superlubricity of ta-C. *Nat. Commun.* **2019**, *10*, 151.

(17) Konicek, A. R.; Grierson, D. S.; Sumant, A. V.; Friedmann, T. A.; Sullivan, J. P.; Gilbert, P. U. P. A.; Sawyer, W. G.; Carpick, R. W. Influence of Surface Passivation on the Friction and Wear Behavior of Ultrananocrystalline Diamond and Tetrahedral Amorphous Carbon Thin Films. *Phys. Rev. B: Condens. Matter Mater. Phys.* **2012**, *85*, 155448.

(18) De Barros Bouchet, M.-I.; Zilibotti, G.; Matta, C.; Righi, M. C.; Vandenbulcke, L.; Vacher, B.; Martin, J.-M. Friction of Diamond in the Presence of Water Vapor and Hydrogen Gas. Coupling Gas-Phase Lubrication and First-Principles Studies. *J. Phys. Chem. C* **2012**, *116*, 6966−6972.

(19) Long, Y.; De Barros Bouchet, M.-I.; Lubrecht, T.; Onodera, T.; Martin, J. M. Superlubricity of Glycerol by Self-Sustained Chemical Polishing. *Sci. Rep.* **2019**, *9*, 6286.

(20) Reichenbach, T.; Mayrhofer, L.; Kuwahara, T.; Moseler, M.; Moras, G. Steric Effects Control Dry Friction of H- and F-Terminated Carbon Surfaces. *ACS Appl. Mater. Interfaces* **2020**, *12*, 8805−8816.

(21) Kuwahara, T.; Moras, G.; Moseler, M. Role of Oxygen Functional Groups in the Friction of Water-Lubricated Low-Index Diamond Surfaces. *Phys. Rev. Mater.* **2018**, *2*, 073606.

(22) Kuwahara, T.; Moras, G.; Moseler, M. Friction Regimes of Water-Lubricated Diamond (111): Role of Interfacial Ether Groups and Tribo-Induced Aromatic Surface Reconstructions. *Phys. Rev. Lett.* **2017**, *119*, 096101.

(23) Dienwiebel, M.; Verhoeven, G. S.; Pradeep, N.; Frenken, J. W. M.; Heimberg, J. A.; Zandbergen, H. W. Superlubricity of Graphite. *Phys. Rev. Lett.* **2004**, *92*, 126101.

(24) Wei, D.; Liu, Y.; Wang, Y.; Zhang, H.; Huang, L.; Yu, G. Synthesis of N-Doped Graphene by Chemical Vapor Deposition and Its Electrical Properties. *Nano Lett.* **2009**, *9*, 1752−1758.

(25) Nijenbanning, G.; Venner, C. H.; Moes, H. Film Thickness in Elastohydrodynamically Lubricated Elliptic Contacts. *Wear* **1994**, *176*, 217−229.

(26) Wagner, C. D.; Naumkin, A. V.; Kraut-Vass, A.; Allison, J. W.; Powell, C. J.; Rumble, J. R., Jr. *NIST Standard Reference Database 20*, version 3.4 (web version), 2003.

(27) Bogdanowicz, R.; Sawczak, M.; Niedzialkowski, P.; Zieba, P.; Finke, B.; Ryl, J.; Karczewski, J.; Ossowski, T. Novel Functionalization of Boron-Doped Diamond by Microwave Pulsed-Plasma Polymerized Allylamine Film. *J. Phys. Chem. C* **2014**, *118*, 8014−8025.

(28) Guo, X.; Rao, L.; Wang, P.; Zhang, L.; Wang, Y. Synthesis of Porous Boron-Doped Carbon Nitride: Adsorption Capacity and Photo-Regeneration Properties. *Int. J. Environ. Res. Public Health* **2019**, *16*, 581.

(29) Kuzharov, A. A.; Luk'yanov, B. S.; Kuzharov, A. S. Tribochemical Transformations of Glycerol. *J. Frict. Wear* **2016**, *37*, 337−345.

(30) Elstner, M.; Porezag, D.; Jungnickel, G.; Elsner, J.; Haugk, M.; Frauenheim, T.; Suhai, S.; Seifert, G. Self-Consistent-Charge Density-Functional Tight-Binding Method for Simulations of Complex Materials Properties. *Phys. Rev. B: Condens. Matter Mater. Phys.* **1998**, *58*, 7260−7268.

(31) Bultinck, P.; Ponec, R.; Van Damme, S. Multicenter Bond Indices as a New Measure of Aromaticity in Polycyclic Aromatic Hydrocarbons. *J. Phys. Org. Chem.* **2005**, *18*, 706−718.

(32) Thomas, A.; Fischer, A.; Goettmann, F.; Antonietti, M.; Müller, J.-O.; Schlögl, R.; Carlsson, J. M. Graphitic Carbon Nitride Materials: Variation of Structure and Morphology and Their Use as Metal-Free Catalysts. *J. Mater. Chem.* **2008**, *18*, 4893−4908.

(33) Wada, N.; Solin, S. A.; Wong, J.; Prochazka, S. Raman and IR Absorption Spectroscopic Studies on α, β, and Amorphous Si_3N_4. *J. Non-Cryst. Solids* **1981**, *43*, 7−15.

(34) Scharpf, R. F. A Compact System for Humidity Control. *Plant Dis. Rep.* **1964**, *48*, 66−67.

(35) Chen, Z.; Liu, Y.; Zhang, S.; Luo, J. Controllable Superlubricity of Glycerol Solution via Environment Humidity. *Langmuir* **2013**, *29*, 11924−11930.

(36) Ferreira, A. G. M.; Egas, A. P. V.; Fonseca, I. M. A.; Costa, A. C.; Abreu, D. C.; Lobo, L. Q. The Viscosity of Glycerol. *J. Chem. Thermodyn.* **2017**, *113*, 162−182.

(37) Stachowiak, G.; Batchelor, A. *Engineering Tribology*, 4th ed.; Butterworth Heinemann, 2013.

(38) Dörr, N.; Brenner, J.; Ristić, A.; Ronai, B.; Besser, C.; Pejaković, V.; Frauscher, M. Correlation Between Engine Oil Degradation,

https://dx.doi.org/10.1021/acsanm.0c03362
ACS Appl. Nano Mater. 2021, 4, 2721−2732

Tribochemistry, and Tribological Behavior with Focus on ZDDP Deterioration. *Tribol. Lett.* **2019**, *67*, 62.
(39) Dörr, N.; Agocs, A.; Besser, C.; Ristić, A.; Frauscher, M. Engine Oils in the Field: A Comprehensive Chemical Assessment of Engine Oil Degradation in a Passenger Car. *Tribol. Lett.* **2019**, *67*, 68.
(40) Köhler, C.; Frauenheim, T. Molecular Dynamics Simulations of CF_x (x = 2, 3) Molecules at Si_3N_4 and SiO_2 Surfaces. *Surf. Sci.* **2006**, *600*, 453−460.
(41) Peguiron, A.; Moras, G.; Walter, M.; Uetsuka, H.; Pastewka, L.; Moseler, M. Activation and Mechanochemical Breaking of C-C Bonds Initiate Wear of Diamond (110) Surfaces in Contact with Silica. *Carbon* **2016**, *98*, 474−483.
(42) Frenkel, D.; Smit, B. *Understanding Molecular Simulation: From Algorithms to Applications*; Academic Press, 2001.
(43) Pastewka, L.; Moser, S.; Moseler, M. Atomistic Insights into the Running-in, Lubrication, and Failure of Hydrogenated Diamond-like Carbon Coatings. *Tribol. Lett.* **2010**, *39*, 49−61.
(44) Lees, A. W.; Edwards, S. F. The Computer Study of Transport Processes under Extreme Conditions. *J. Phys. C: Solid State Phys.* **1972**, *5*, 1921−1929.
(45) Peters, E. A. J. F. Elimination of Time Step Effects in DPD. *Europhys. Lett.* **2004**, *66*, 311−317.
(46) Berendsen, H. J. C.; Postma, J. P. M.; van Gunsteren, W. F.; DiNola, A.; Haak, J. R. Molecular Dynamics with Coupling to an External Bath. *J. Chem. Phys.* **1984**, *81*, 3684−3690.
(47) Humphrey, W.; Dalke, A.; Schulten, K. VMD: visual molecular dynamics. *J. Mol. Graphics* **1996**, *14*, 33−38.
(48) Stukowski, A. Visualization and analysis of atomistic simulation data with OVITO –the Open Visualization Tool. *Modell. Simul. Mater. Sci. Eng.* **2010**, *18*, 015012.
(49) Walsh, P.; Omeltchenko, A.; Kalia, R. K.; Nakano, A.; Vashishta, P.; Saini, S. Nanoindentation of Silicon Nitride: A Multimillion-Atom Molecular Dynamics Study. *Appl. Phys. Lett.* **2003**, *82*, 118−120.
(50) Jülich Supercomputing Centre. JUWELS: Modular Tier-0/1 Supercomputer at the Jülich Supercomputing Centre. *Journal of Large-Scale Research Facilities* **2019**, *5*, A135.

https://dx.doi.org/10.1021/acsanm.0c03362
ACS Appl. Nano Mater. 2021, 4, 2721−2732